Applied Thermal Engineering 181 (2020) 116030

Contents lists available at ScienceDirect

Applied Thermal Engineering

journal homepage: www.elsevier.com/locate/apthermeng

Heat transfer coefficients of additively manufactured tubes with internal pin fins for supercritical carbon dioxide cycle recuperators☆

Matthew Searle [a,*], Jim Black [b], Doug Straub [c], Ed Robey [d], Joe Yip [c], Sridharan Ramesh [d], Arnab Roy [d], Adrian S. Sabau [e], Darren Mollot [f]

[a] US Department of Energy Postgraduate Research Program, National Energy Technology Laboratory, 3610 Collins Ferry Rd, Morgantown, WV 26505, United States
[b] US Department of Energy, National Energy Technology Laboratory, Pittsburgh, PA, United States
[c] US Department of Energy, National Energy Technology Laboratory, Morgantown, WV, United States
[d] Leidos Research Support Team, Morgantown, WV, United States
[e] Computational Sciences & Engineering Division, Oak Ridge National Laboratory, Oak Ridge, TN, United States
[f] US Department of Energy, Washington, DC, United States

ARTICLE INFO

Keywords:
Supercritical carbon dioxide
Recuperator
Enhanced heat transfer
Additive manufacturing
Helical pin fins

ABSTRACT

This paper describes the measurement of convective heat transfer coefficients and friction factors for sCO_2 flowing in additively manufactured tubes with internal pin fins at the US DOE's National Energy Technology Laboratory in Morgantown, WV. The measurement procedures were validated by conducting benchmark tests with smooth stainless-steel tube and comparing the results with published correlations for Nusselt number (*Nu*) and friction factor. Over Reynolds numbers (Re_D) ranging from 5×10^4 to 2.5×10^5, measured *Nu* was within 5% of the Dittus-Boelter correlation and measured friction factors were within 5% of the McAdams correlation for smooth tube flow.

The candidate pin fin patterned pipes were additively manufactured (AM) at the Oak Ridge National Laboratory. The pins were circular or elliptical in cross-section and were printed at a 30° angle relative to the inner wall (to meet AM constraints). The pin arrangement was helical to promote enhanced heat transfer due to swirl flow. Pin length to diameter aspect ratio was 1.33, 2, and 8, while the pin diameter to tube diameter ratio was 0.188, 0.125, and 0.063. Tests were performed for Re_D varying from 6.9×10^4 to 2.2×10^5 and at conditions equivalent to the low pressure (LP) outlet (8.69 MPa, 361 K) and the high pressure (HP) inlet (20.7 MPa, 350 K) of the low temperature recuperator (LTR) in an indirect sCO_2 cycle. The Wilson plot technique was utilized to measure the bulk heat transfer coefficients.

For the best performing design (tube A, pin length to tube diameter ratio: 1.33, pin diameter to tube diameter ratio: 0.19), the local heat transfer coefficient increased by 136% relative to the Dittus-Boelter correlation at the LTR low pressure outlet and 194% at the LTR high pressure inlet. These correspond to a 282% and a 271% increase in the product of the heat transfer coefficient and surface area (adjusted for fin efficiency) product, respectively. Large pressure drops across the test articles were observed. For Tube Design A, the average friction factor, across the range of Re_D considered, was significantly larger than the McAdams correlation at both the LTR LP outlet and the LTR HP inlet. A thermal performance factor was utilized to express the ratio of material required to build a finned heat exchanger relative to a finless heat exchanger with the same heat duty and pumping power. Tube Design A was estimated to decrease the required heat exchanger material by 13%.

☆ **Notice**: This manuscript has been authored in part by UT-Battelle, LLC, under contract DE-AC05-00OR22725 with the US Department of Energy (DOE). The United States Government retains and the publisher, by accepting the article for publication, acknowledges that the United States Government retains a non-exclusive, paid-up, irrevocable, world-wide license to publish or reproduce the published form of this manuscript, or allow others to do so, for United States Government purposes. The Department of Energy will provide public access to these results of federally sponsored research in accordance with the DOE Public Access Plan (*http://energy.gov/downloads/doe-public-access-plan*).

* Corresponding author.
E-mail addresses: matthew.searle@netl.doe.gov (M. Searle), james.black@netl.doe.gov (J. Black), douglas.straub@netl.doe.gov (D. Straub), edward.robey@netl.doe.gov (E. Robey), m.yip@netl.doe.gov (J. Yip), sridharan.ramesh@netl.doe.gov (S. Ramesh), arnab.roy@netl.doe.gov (A. Roy), sabaua@ornl.gov (A.S. Sabau), darren.mollot@hq.doe.gov (D. Mollot).

https://doi.org/10.1016/j.applthermaleng.2020.116030
Received 12 May 2020; Received in revised form 10 August 2020; Accepted 7 September 2020
Available online 12 September 2020

1. Introduction

Presently there is worldwide interest in sCO_2 power generation technology as it has the potential to offer a five-percentage point increase in cycle efficiency and an order of magnitude decrease in turbomachinery volume relative to conventional steam Rankine cycles. The five-percentage point increase in efficiency corresponds to an 11% increase from a steam Rankine cycle efficiency of 45% to an indirect sCO_2 recompression Brayton cycle efficiency of 50%, with both cycles operating at a turbine inlet temperature of 700 °C [1]. Thermodynamic models for direct and indirect sCO_2 cycles have been considered. A direct cycle combusts fuel in an oxygen-rich environment and uses the combustion products as the working fluid. The indirect cycle adds heat to a nearly pure carbon dioxide stream through a heat exchanger as shown in Fig. 1. The heat can originate from any source such as fossil, solar, or nuclear. Both cycles are based on the recuperated Brayton cycle [2,3]. Although the results of the present study consider heat transfer at conditions in the indirect Brayton cycle, the concepts presented are applicable for both cycles.

Both direct and indirect sCO_2 cycles require significant recuperation (3–4 times net plant output), which is very expensive to attain [4]. Thus, cost-effective recuperators are required [4]. For a given heat exchanger manufacturing technology, the capital cost of the heat exchanger equipment scales with the material volume. The material volume may be reduced through strategies for enhancing heat transfer from the hot stream to the cold stream. One strategy is the addition of internal heat transfer enhancement features, which increase the heat transfer through larger internal surface area and larger heat transfer coefficients. This strategy is successful when the heat exchanger material volume decreases significantly, while still achieving the same heat duty and pressure drop. The criterion for decreased material volume is that the heat transfer enhancement is sufficiently large relative to the increase in pressure drop, as discussed in Section 2.6.

Nomenclature

A	tube internal area
A_n	smooth tube internal surface area per unit length
A_a	finned tube internal surface area per unit length
A_s	secondary (finned) area
A_p	primary (finned) area
D	inner diameter of tube
d	major diameter of pin fin
f	friction factor
G	tube mass flux
h	heat transfer coefficient
k_f	fluid thermal conductivity
k_m	metal thermal conductivity
L	tube length
$LMTD$	log mean temperature difference across heat exchanger
$\dot{m}$	mass flow rate
M	material volume per unit length
Nu	Nusselt number, $Nu = hD/k_f$
p	pitch of helix
P	test condition pressure
P_f	fin perimeter
Pr	Prandtl number
Q	heat transfer rate
R_a	surface roughness (arithmetic average)
R_{ov}	overall thermal resistance of heat exchanger
R_{ku}	kurtosis (roughness parameter)
R_q	surface roughness (root mean square)
R_{sk}	skewness (roughness parameter)
R_w	wall thermal resistance
R_z	mean roughness depth
R	thermal resistance
Re_D	Reynolds number based on tube diameter, $Re_D = GD/\mu$
s	spacing of pin fins along helix, scaled by pin fin major diameter
T	test condition temperature
U	overall conductance of heat exchanger, relative to internal heat transfer area
V	material volume for finned tube
x_1	pin semimajor radius
x_2	pin semiminor radius
y'	fin vertical height

Greek Variables

α	pin angle
ΔP	pressure drop across tube
$\in$	sand grain roughness
η	overall surface efficiency
η_f	fin efficiency
μ	dynamic viscosity
$\overline{\mu}$	arithmetic mean
ν	fin equation parameter
ρ	fluid density
σ	standard deviation

Subscripts

0	finless (smooth) tube (if no subscript "0″, with respect to finned tube)
c	cold side (tube)
h	hot side (shell)

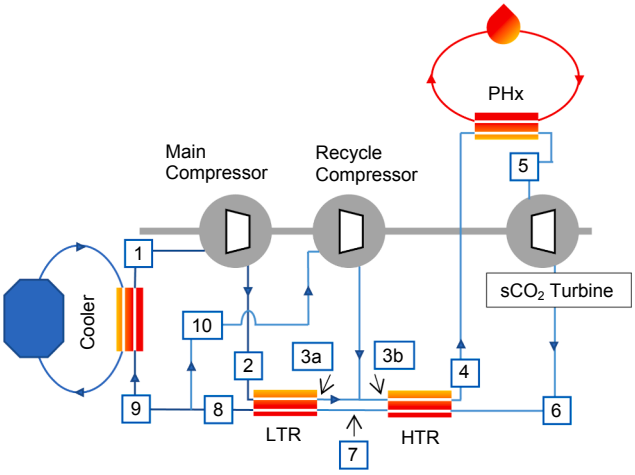

Fig. 1. Schematic of an indirect sCO_2 cycle showing the primary heat exchanger (PHx), turbine, high temperature recuperator (HTR), low temperature recuperator (LTR), cooler, main compressor, and recycle compressor. The cycle points are numbered.

Two heat exchanger technologies that are being considered for implementation in sCO_2 power cycles are: (1) printed circuit heat exchangers (PCHE), and (2) shell-and-tube heat exchangers. Since heat

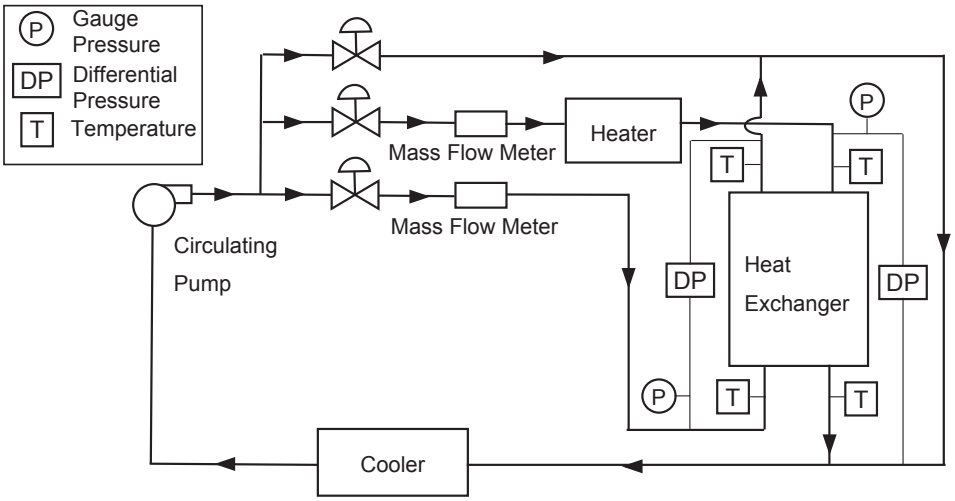

Fig. 2. Block diagram of NETL HEET rig.

transfer coefficients increase as tube hydraulic diameter increase, there has been a trend to consider shell-and-tube heat exchangers with smaller tube diameters. These so-called "microtube and shell heat exchangers" utilize small tubes with hydraulic diameters on the order of a millimeter.

PCHE have received significant attention [5–7]. One-dimensional models of PCHE were previously developed at NETL for design and dynamic analysis. These models were previously validated with experimental data from the Naval Nuclear Laboratory and then utilized to design and model recuperators for a 10 MWe supercritical recompression Brayton cycle. Both PCHE and, micro shell and tube heat exchangers, were considered [8–9]. The PCHE design had metal masses slightly larger than the micro tube shell-and-tube heat exchanger design but the authors noted that the PCHE design was attractive due to mature PCHE manufacturing technology and significant industrial experience.

Micro tube and shell heat exchangers have also received attention. A recent project designed and tested a microtube tube and shell prototype and found that manufacturing processes limited the approach [10]. Present PCHE designs have higher thermal performance than conventional shell-and-tube heat exchangers. However, heat transfer enhancement features for conventional heat exchangers, such as shell-and-tube heat exchangers, which were previously challenging to manufacture by conventional processes can now be manufactured by additive manufacturing (AM).

The present work considers a novel helical patterned pin fin geometry with the intent to determine if the heat exchanger heat transfer would increase without an excessive increase in the pressure drop. The helical pattern enhances heat transfer by creating swirl flow, while the pinned pattern promotes mixing through vortex shedding. This geometry cannot be fabricated without additive manufacturing and, thus, has received no prior attention in the literature.

AM enhanced heat transfer features in shell and tube heat exchangers may increase their thermal performance to exceed that of PCHE. Further, additive manufacture will allow enhanced shell-and-tube heat exchangers to be fabricated in a single build. Thus, additively manufactured shell-and-tube technology could replace the etch, diffusion bonding, and manifold welding steps required to fabricate PCHE.

Other benefits of additively manufactured shell and tube heat exchangers for use in supercritical carbon dioxide cycles include lower pressure drop, decreased weight, customizability, enhanced heat transfer resulting from the AM process surface roughness, and decreased cost.

To characterize the benefit of including additively manufactured internal fins on the heat exchanger performance, it is necessary to measure the heat transfer coefficient on the inside of the tube with internal pin fins.

This is accomplished through the Wilson plot technique, which allows experimental measurement of heat transfer coefficients on the hot or cold side of a heat exchanger. The Wilson plot technique consists in keeping the thermal resistance constant on one side of the heat exchanger (reference side) while varying the thermal resistance (by changing the flow rate) on the side where the heat transfer coefficient is measured. Wilson first introduced the technique for scenarios where there was a high heat transfer coefficient (typical of boiling or condensation) on the reference side [11]. Later, the Wilson plot technique was modified to consider scenarios where the requirement of a large heat transfer coefficient on the reference side was relaxed [12]. In this scenario, the heat transfer coefficient of the test side is obtained by varying the flow rate of the test side, while maintaining the thermal resistance on the reference side constant by controlling the reference side flow rate and average temperature [4,12–13]. In this study, we utilize the modified Wilson plot method to measure the heat transfer coefficient at the tube side of the test article.

Fig. 3. Photograph of NETL HEET rig.

2. Experiment and data analysis

2.1. Experimental facility

The NETL Heat Exchange and Experimental Testing (HEET) rig at the U.S. DOE's National Energy Technology Laboratory is a closed loop,

Table 1
Table of dimensional parameters for all tubes considered.

	Tube A	Tube B	Tube C	Conv. Tube	Welded Conv.	Finless AM Tube
Tube ID (mm), D	7	7	7	7	7	7
Tube OD (mm)	9.5	9.5	9.5	9.5	9.5	9.5
Ellipse Major Diameter (mm), d	0.75	0.5	1.50			
Aspect Ratio (Major/Minor)	1	1	6			
Pin Length (mm)	1.75	1.75	3.51			
Pin Angle from Tube Wall	30°	30°	30°			
Major Diameter Angle to Flow	60°	60°	60°			
Number of Helix Paths	4	4	4			
Pin Helical Spacing, s/d	2	2	2			
Dimensionless Helix Pitch, p/D	2	2	2			
Fin Cross Sectional Area (mm^2)	0.44	1.96	0.29			
Pins per Axial Length (number/mm)	6	9	3			
A/A_0	1.8	1.8	2.32	1	1	1
M/M_0	1.12	1.08	1.08	1	1	1
Total Length (mm)	635	635	635	152	635	635
Segment Length (mm)	127	127	127	N/A	127	127
Welded	Yes	Yes	Yes	No	Yes	Yes

sCO_2 heat exchanger test rig [4]. In the present test, the rig was utilized to measure tube-side heat transfer coefficients in a sCO_2 single-pass, counter-flow heat exchanger. The inlets and outlets of the heat exchanger were instrumented so that the inlet and outlet temperatures were measured as well as the differential pressures and inlet gauge pressures. A block diagram of the system is shown in Fig. 2 and a photograph is displayed in Fig. 3.

The flow is circulated using a Parker/Autoclave Engineering 5.6 kW (7.5 horsepower) variable speed, magnetically coupled, centrifugal pump. After leaving the circulating pump, the flow loop divides into three streams. The first stream (moving from top to bottom in Fig. 2) is a bypass loop which was not utilized for these tests. The flow in the second and third streams are controlled with automated valves and instrumented with Coriolis mass flow meters (Micro Motion, ±0.5% full scale). The second stream (hot stream) passes through tube sections wrapped with wire coil heaters before entering the shell-side of the heat exchanger. The power input to these heaters is controlled to maintain a constant average temperature for the hot (reference) CO_2 in the heat exchanger. The third stream (cold stream) passes through the tube-side of the heat exchanger. After the test section, all three streams join and pass through a cooler, which is a water-cooled, tube-in-tube heat exchanger. Following the cooler, the stream is directed to the inlet of the circulating pump.

Capabilities of the HEET rig include pressure to 24 MPa (3,500 psia), temperature to 811 K (1,000°F), mass flow rate to 1.5 kg/s (3 lbm/s), and Re to 500,000 for pipe inner diameters of 7 mm. In its present state, the maximum operating temperature on the cold fluid side is limited to 477 K (400°F) due to the maximum allowable temperature for the Coriolis flow meters and 671 K (750°F) on the hot fluid side due to the maximum allowable tube temperature.

Class A resistance temperature detectors are used for temperature measurement. The transducers were immersed in the working fluid 10–15 probe diameters. Fisher/Rosemount transducers are used for pressure and differential pressure measurement. A Teledyne ISCO

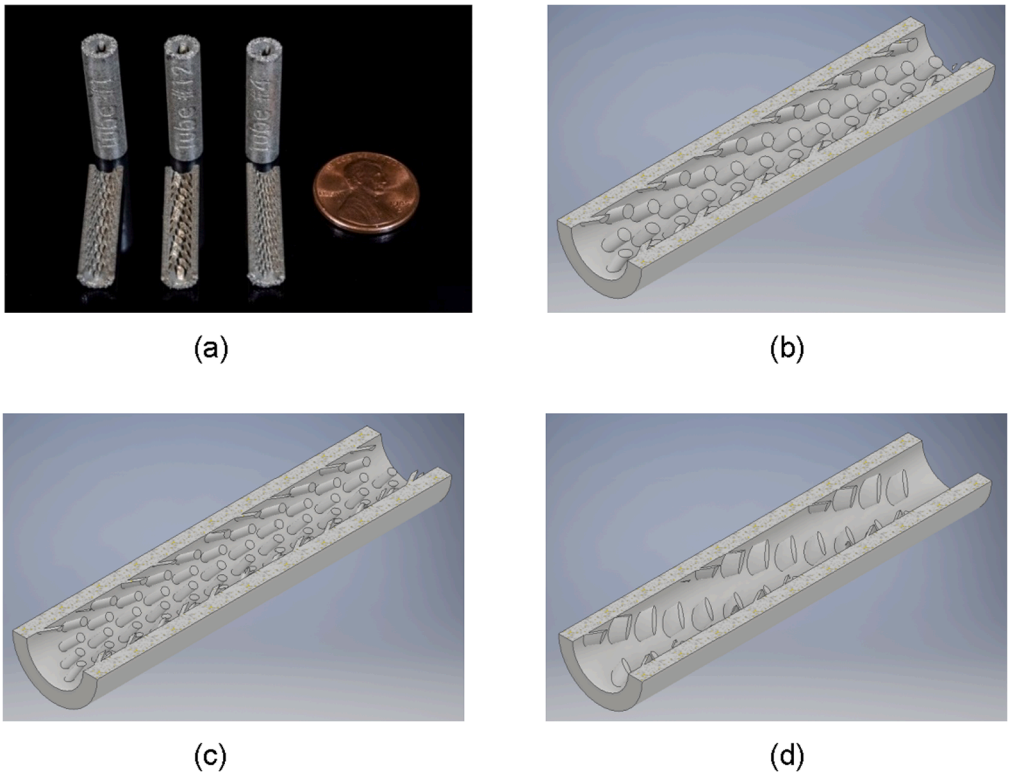

Fig. 4. (a) Sectioned and non-sectioned helical pin–fin patterned tubes are shown for the three designs (A, B, and C) considered in this study. (b-d) CAD models of the pin fin designs, A, B, and C, respectively.

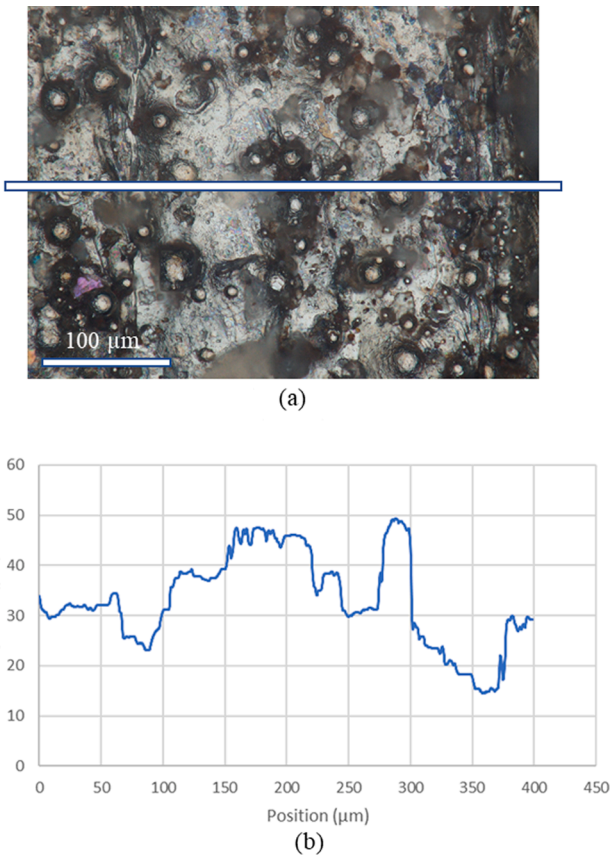

Fig. 5. Example of sample surface roughness: (a) AM surface using a white light interferometer (b) Surface profile acquired along the horizontal line shown at (a).

syringe pump (not shown) is used to charge the system with CO_2. Prior to filling the system to the operating pressure, all air is removed by purging the system three times with CO_2.

2.2. Test articles

Six tube designs were considered:

1. a conventional seamless tube
2. a tube composed of welded segments (referred to as the "welded conventional tube")
3. a tube composed of finless AM tube segments
4. a tube composed of welded AM Tube Design A segments
5. a tube composed of welded AM Tube Design B segments
6. a tube composed of welded AM Tube Design C segments

All test articles were made of 316 stainless steel. The tubing had an inner diameter of 7 mm (0.275 in.) and a wall thickness of 1.2 mm (0.049 in.). The AM test articles were fabricated using the laser powder bed process on the Renishaw AM250 system at the Oak Ridge National Laboratory.

The tube length was limited to 127 mm (5 in.) due to limitations in the AM volume chamber. To create a test article, five tubes were joined by orbital welding. All heat exchanger lengths were 0.64 m (2.1 ft) except for the conventional tube which was 1.52 m (5 ft).

Dimensional parameters for the Tube Designs A, B, and C are shown in Table 1. Relative to Tube A, Tube B has a smaller diameter fin and Tube C has a longer length fin and larger fin aspect ratio. A and A_0 are the internal surface area for finned and finless tubes, respectively. M and M_0 are the tube material volume per unit length for finned and finless tubes, respectively. We note that the pin helical spacing and the helix pitch are nondimensional. The pin helical spacing, s, is scaled by the pin major diameter and the helix pitch, p, is scaled by the tube inner diameter.

Table 2
Surface roughness parameters for AM manufactured finless tube, average and standard deviation ($\bar{\mu} \pm \sigma$).

R_a (µm)	R_q (µm)	R_z (µm)	R_{sk}	R_{ku}
4.4 ± 1.1	5.5 ± 1.4	21.4 ± 5.7	0.34 ± 0.50	2.64 ± 0.67

Table 3
Test condition parameters considered in the present study.

Test Condition	Cycle Point	Location	T (K (°F))	P (MPa (psia))	***Re*** range of test condition (cold)
I	8	LTR, LP Outlet	361 (190)	8.69 (1260)	75 k–250 k
II	2	LTR, HP Inlet	350 (170)	20.7 (3000)	75 k–250 k

In Fig. 4 panel (a), sectioned and non-sectioned samples of Tube Designs A, B, and C are shown. Note that these tubes are 4:7 scale reproductions of the experimental tubes and have shorter lengths. In panels (b-d) CAD models of the tubes are displayed.

2.3. Surface roughness characterization

Three-dimensional surface roughness profiles were acquired using a white light interferometer (Olympus DSX510). A typical microscope image and surface elevation profile are shown in Fig. 5. As visible in the photomicrograph and profile, one important feature of the AM surface roughness are sintered particles, which have a particle size which varies from 15 µm to 45 µm. The average line roughness metrics ($R_a, R_q, R_z, R_{sk}, R_{ku}$) and their standard deviations are reported in Table 2. The roughness parameters were calculated for each profile and then averaged across 14 samples. This surface roughness characterization procedure was selected following the approach outlined by Stimpson et al. [14]. In Appendix A, we report the expressions for calculating these parameters.

2.4. Test methodology

The test conditions selected for this study are the LP outlet and HP inlet in the LTR. In the HEET rig, these conditions are applied to the cold (tube) side inlet. As shown in Table 3, the LP outlet of the LTR (cycle point 8 – see Fig. 1) was test condition I. The HP inlet of the LTR (cycle point 2) was test condition II.

The HEET system was purged and charged with carbon dioxide to the test pressure before acquiring the data. Simultaneously, the system was heated to the test condition temperature. Careful manual control of the system pressure, heater temperature setpoint, cooling water flow rate, and hot stream and cold stream mass flow rates was required to ensure control points were reached and remained stable. Following a test plan, the cold side flow rate on the tube side was varied while maintaining a constant hot side flow rate (shell side) and constant average hot side temperature. The hot side average heater temperature was determined by estimating the hot inlet temperature necessary to reach the desired operating conditions, heating the system to this condition, recording the average hot side temperature setpoint required to reach the condition, and using this setpoint for all subsequent tests. Steady state operation was assured by waiting before recording data until the standard deviation in the pressure drop was less than 0.069 kPa (0.01 psi).

2.5. Data reduction and analysis

The current study relies on the Wilson plot technique applied to a

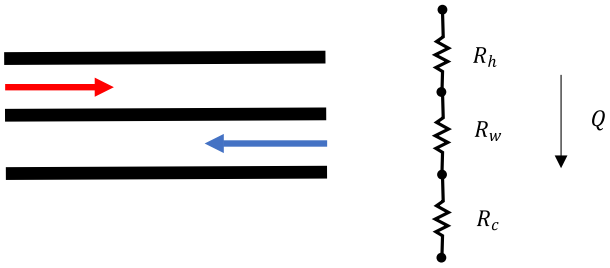

Fig. 6. Schematic illustration of resistance network considered.

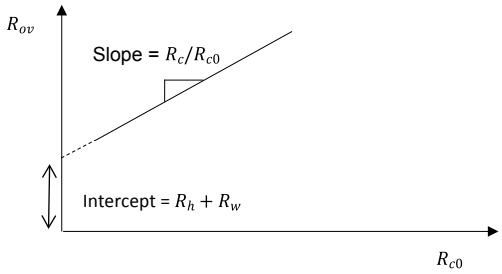

Fig. 7. Schematic illustration of a Wilson plot.

heat exchanger model to obtain the heat transfer coefficient at the cold (tube) side [4,12–13]. Under conditions of small property variations, negligible conjugate conduction, and small heat transfer to the environment, the rate of heat transfer (Q) from the hot fluid to a cold fluid in a heat exchanger is:

$$Q = U \times A \times LMTD = \frac{LMTD}{R_{ov}} \tag{1}$$

where U is the overall conductance (relative to the tube side area), A is the heat transfer area at the tube side, and $LMTD$ is the log mean temperature difference (measured between the inlets and outlets of the tube and shell) [15]. $R_{ov} = 1/UA$ is the total resistance between the hot and cold streams. Rearranging Eq. (1) yields the overall resistance

$$R_{ov} = \frac{LMTD}{Q} \tag{2}$$

The overall resistance between the hot stream and the cold stream is the sum of convection resistance at the cold side wall (R_c), conduction resistance in the tube wall (R_w), and convection resistance at hot side wall (R_h).

$$R_{ov} = R_c + R_w + R_h \tag{3}$$

The thermal resistance network is schematically illustrated in Fig. 6.

The convection resistances are expressed as $R_c = 1/\eta h_c A_c$ and $R_h = 1/h_h A_h$ where h_c is the heat transfer coefficient at the cold side, A_c is the cold side area, h_h is the heat transfer coefficient at the hot side, and A_h is the hot side area. R_c, R_w, and R_h are each unknown. However, R_{ov} can be calculated from experimental temperature measurements utilizing Eq. (2). The experiments are performed so that R_c varies while R_w and R_h remain constant. This is achieved by varying the mass flow rate on the cold side while controlling the mass flow rate and average temperature on the hot side, as stated at Section 2.1.

Even though R_c is unknown, one can calculate a cold side resistance value, R_{c0}, with the heat transfer coefficient calculated from the Dittus-Boelter relationship for a heated, fully-developed internal flow, which is given, as:

$$Nu_0 = 0.023 Re_D^{0.8} Pr^{0.4} \tag{4}$$

where $Nu_0 = h_c D/k_f$ will serve as the baseline Nusselt number, $Re_D = GD/\mu$ is the Reynolds number based on the tube internal diameter, and Pr is the Prandtl number. Here, h_c is the cold side heat transfer coefficient. k_f is the fluid conductivity. G is the average mass flux. μ is the dynamic viscosity. The fluid properties are estimated at average temperature and pressure inside the tube using NIST REFPROP [16] and which implements the Span-Wagner equation of state [17]. R_{c0} is calculated with $h_c = h_0$ and $A_c = A_0$

$$R_{c0} = \frac{1}{h_0 A_0} = \frac{D}{Nu_0 k_f A_0} \tag{5}$$

where A_0 is the smooth (finless) tube area and h_0 is the heat transfer coefficient as calculated with the Dittus-Boelter correlation (Eq. (4)). It must be emphasized that h_0 is defined with respect to the finless tube surface area, A_0. Assuming that R_{c0}/R_c is a constant, Eq. (3) can be expressed as:

$$R_{ov} = \left(\frac{R_c}{R_{c0}}\right) R_{c0} + R_w + R_h \tag{6}$$

The Wilson plot is now formed by plotting R_{ov} as a function of R_{c0}. Such a plot is shown schematically in Fig. 7. It must be emphasized that (R_c/R_{c0}) is the slope of the line and the y-intercept is $R_w + R_h$. If the calculated values, R_{c0}, equal the unknown experimental value, R_c, then $R_c/R_{c0} = 1$ and the R_{ov} vs. R_{c0} line has a slope of 1. Otherwise, the R_c/R_{c0} value can be used to calculate Nu/Nu_0.

At this point, it is important to consider if the assumption that R_{c0}/R_c is a constant is valid and how the approximation may be validated. If $R_{c0}/R_c$is constant, then the Wilson plot will have no curvature. However, if a curve is recorded experimentally, then the assumption of constant R_{c0}/R_c must be re-evaluated. For all results presented in this work, negligible curvature was observed in the Wilson plots.

An expression similar to Eq. (5) can be obtained for the finned tube with $h_c = h$ and $A_c = A$, yielding $R_c = D/(Nuk_f A)$. It must be emphasized that h is the heat transfer coefficient in the finned tube with respect to the finned surface area, A. Taking the ratio of R_c to R_{c0} yields

$$\frac{R_c}{R_{c0}} = \frac{D}{\eta A k_f Nu} \frac{A_0 k_f Nu_0}{D} = \frac{A_0 Nu_0}{\eta A Nu} \tag{7}$$

Rearranging yields,

$$\frac{Nu}{Nu_0} = \frac{R_c}{R_{c0}} \frac{\eta A}{A_0} \tag{8}$$

Thus, the Nusselt number ratio (Eq. (8)) may be determined iteratively with the Wilson plot line slope (R_c/R_{c0}), the ratio of A to A_0, and a formula which provides the overall surface efficiency as a function of the heat transfer coefficient

$$\frac{Nu}{Nu_0} = \frac{R_c}{R_{c0}} \frac{\eta A}{A_0} \tag{9}$$

The overall surface efficiency is a function of the fin efficiency and the surface primary and secondary areas.

The efficiency of an angled elliptical pin fin, η_f, (Appendix C) is given

$$\nu^2 = \frac{P_f h}{k_m A_c \cos(\alpha)} \sqrt{\frac{1 + (x_2/x_1)^2/\cos(\alpha)^2}{1 + (x_2/x_1)^2}} \tag{10}$$

$$\eta_f = \frac{1}{\nu y'} \frac{\left(\sinh(\nu y') + \frac{k\cos(\alpha)\nu}{h}\cosh(\nu y')\right)}{\left(\cosh(\nu y') + \frac{k\cos(\alpha)\nu}{h}\sinh(\nu y')\right)} \tag{11}$$

where y' is the fin vertical height, α is the fin angle, k is the fin material thermal conductivity, h is the heat transfer coefficient, P is the fin perimeter, A_c is the fin cross sectional area, x_1 is the ellipse major semidiameter, and x_2 is the ellipse minor semidiameter.

The overall surface efficiency is expressed

$$\eta = \frac{A_s\eta_f + A_p}{A_s + A_p} \tag{12}$$

where A_p is the primary (non-finned) surface area and A_s is the secondary (finned) surface area.

An experimental study of a heat exchanger is incomplete without reporting the pressure drop of the heat exchanger. The tube-side pressure drop is reported in terms of its friction factor

$$f = \frac{\pi^2}{8}\frac{\Delta P \rho D^5}{L\dot{m}^2} \tag{13}$$

where ΔP is the pressure drop across the tube, L is the length of the tube, D is the tube inner diameter, ρ is the density of the fluid in the tube evaluated at the average temperature and pressure, and $\dot{m}$ is the mass flow rate in the tube [18]. A reference friction factor for turbulent flow in a smooth tube is calculated using the McAdams correlation

$$f_0 = 0.184 Re_D^{-0.2} \tag{14}$$

which is valid for $3\text{x}10^4 < Re_D < 2 \times 10^6$. This value is utilized to estimate f/f_0.

2.6. Thermal performance factor

A barrier to market acceptance of indirect supercritical carbon dioxide power cycles is the expense of heat exchangers. sCO_2 cycles require high and low temperature recuperators, a primary heater, and a cooler. The heat duty in these recuperators is large [4]. One route to reduce the cost of these heat exchangers is to additively manufacture them. The means of cost reduction would be a dramatic decrease in volume of required heat exchanger material (not yet shown experimentally) and the potential for reduced labor expenses.

Both the Nusselt number and the friction factor increase due to the introduction of the pin fins. The material volume required to make a heat exchanger with the same heat duty and pressure drop will decrease if the introduction of pin fins yields an increase in the internal ηhA, which is sufficiently large relative to increase in pressure drop. A thermal performance factor needs to be introduced to capture this relationship. Such parameters allow the optimization of one performance characteristic (e.g. heat load, friction power, material volume) of the heat exchanger while the other performance characteristics are constrained [19].

A candidate thermal performance factor is the classical parameter, $TPF = (Nu/Nu_0)/(f/f_0)^{1/3}$. This performance factor indicates how much the heat transfer rate will increase when internal fins are added if the finned and finless heat exchangers have the same surface area and the same pumping power [19]. However, an examination of the derivation of this parameter shows that it provides no information on the change in material volume of the heat exchanger [20]. Clearly, the classical thermal performance factor is the incorrect objective for minimizing the heat exchanger material volume while all other parameters are kept constant.

Thus, a thermal performance factor is selected, which minimizes volume while keeping both the heat duty and pumping power constant [18]. If the thermal resistance of the outer heat exchanger surface is small (Appendix B), this performance factor is expressed, as:

$$\frac{V}{V_0} = \frac{(f/f_0)^{1/2}}{(\eta Nu/Nu_0)^{3/2}}\frac{A_n}{A_a}\frac{M}{M_0} \tag{15}$$

where V is the total material volume with fins, V_0 is the total material volume without fins. A_a and A_n are the internal surface area per unit length of finned and finless tubes, respectively.

It is important to differentiate the notation A_a and A_n from A and A_0. The latter equals the total internal surface area, while the former equals the total internal surface area per unit length. A_a is related to A and A_n is related to A_0 by the relationships, $A = NLA_a$ and $A_0 = N_nL_nA_n$. The ratio, A/A_0, may differ from the ratio, A_a/A_n when the number, N, or segment length, L, of parallel internal flow paths for the finned and finless heat exchangers are different. This nomenclature is retained to maintain consistency with the prior derivation [19].

The derivation of V/V_0 is provided in Appendix B with minor modifications from its original derivation [19]. This derivation also yields the classical thermal performance factor under the constraint of equal surface area and pressure drop.

Table 4
Uncertainties of measured variables.

Measurement	Uncertainty	Manufacturer	Model
Temperature (°C)	±(0.15 + 0.002T)	TEMPCO	RTD2-SA3FC060KM00
Pressure	±0.2% measured value	ROSEMOUNT	3051TG4A2B21AB4E5Q4
Differential Pressure	±0.2% measured value	ROSEMOUNT	3051S1CD3A2E12A1AB4E5Q4
Mass Flow Rate	±0.25% measured value	MICRO MOTION	CMFS050P319N4BAE2CZZ
Tube Length	±6.35 mm (0.25 in)	N/A	N/A
Tube Diameter	±0.25 mm (0.01 in)	N/A	N/A

2.7. Uncertainty analysis

An analysis was performed to determine the uncertainty in each dependent variable calculated from measured variables. This analysis, shown in a general form here, was applied to the Nusselt number, the friction factor, the ratios of each parameter relative to the smooth tube correlation, and the thermal performance factor. The uncertainty analysis is outlined generally. A result calculated from measured variables may be expressed as a function of those variables

$$y = f(x_1, x_2, \cdots, x_i, \cdots, x_n)$$

where x_i are measured experimental variables, y is the calculated variable, and the function f may be expressed analytically or numerically.

In general, the uncertainty in a result calculated from measured experimental variables may be determined by multiplying the error of each measured variable by the derivative of the function with respect to that variable evaluated at the operating conditions and combining the errors by summing the square of each contribution.

$$u_y = \sqrt{\sum_{i=1}^{n}\left(\frac{\partial y}{\partial x_i}u_i\right)^2} \tag{16}$$

where u_i are the associated uncertainties in each variable. Uncertainties for the temperature, pressure, differential pressure, and mass flow rate instruments are provided in Table 4.

Determining the propagation of error through the Wilson plot technique and the friction factor calculation is important to interpreting the results of the present work, thus the uncertainty analysis was applied to each, utilizing analytical derivatives for the friction factor and a numerical approach for the Nusselt number.

The error in f/f_0 was estimated utilizing the Kline and McClintock method. The approach estimates the uncertainty in a calculated value as the square root sum of squares of contributions to uncertainty from each input variable in the expression for the calculated variable [21]. When estimating the error in the friction factor, instrumentation/measurement errors in pressure drop, tube side mass flow rate, pipe diameter, and length of the pipe were considered.

The friction factor calculation is a function of pressure drop, tube

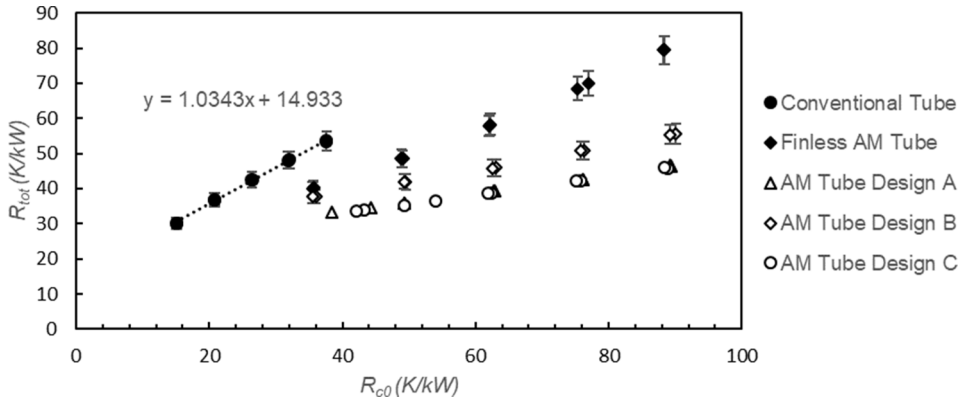

Fig. 8. Wilson plot for test condition I ($79\mathbf{k} < \boldsymbol{Re_D} < 246\mathbf{k}$).

length and tube diameter, cold side temperature, and cold mass flow. The pressure drop uncertainty is dominated by uncertainty in the tube diameter. This analysis yielded an uncertainty of ± 5% in f/f_0 (95% confidence interval). Since it is challenging to calculate analytical derivatives for the Wilson plot analysis, a sequential perturbation technique [22] was utilized in place of the Kline and McClintock method to estimate Nu/Nu_0. In sequential perturbation, the Nusselt number is calculated with one input variable increased by its error (perturbed) and the other variables held constant. Then, the variable is decreased by its error and the Nusselt number is calculated again. The error in the Nusselt number resulting from these calculations is averaged. The calculations are repeated for each variable and the result is recorded. The overall error in the Nusselt number is the square root sum of squares of the perturbation errors. An uncertainty analysis for the Nusselt Number was performed and included the cold inlet temperature, cold outlet temperature, cold mass flow, cold side pressure, hot inlet temperature, and hot outlet temperature. The Nusselt number uncertainty was dominated by the inlet and outlet cold side temperatures. This approach yielded a 15% uncertainty in Nu/Nu_0, each at 95% confidence intervals.

The Kline and McClintock method was utilized again to estimate the uncertainty in the thermal performance factor, V/V_0, combining the uncertainties from the f/f_0 and Nu/Nu_0 error analyses, yielding a ± 13% uncertainty in V/V_0 (95% confidence interval). Uncertainty in the thermal performance factor, (V/V_0) was determined utilizing the uncertainty in η, Nu/Nu_0, and f/f_0 and was dominated by uncertainty in Nu/Nu_0.

To verify that the welds did not influence the results, a conventional tube was cut into five segments and welded back together. Tests were performed on this article and the difference in Nusselt number ratio, Nu/Nu_0, was less than 10%.

3. Results and discussion

The first set of results to be discussed are the Wilson plots that are displayed along with pressure drop per unit length. This will be followed by a discussion on the heat transfer enhancement (increase in heat duty). Finally, consideration is given to how much the addition of enhanced internal surfaces can reduce the heat exchanger material.

3.1. Wilson plot

The Wilson plot, as introduced in the analysis section, is a graphical method of determining the heat transfer coefficient on either the hot or cold side of a heat exchanger. In this work, the cold side (tube side) of a single pass shell and tube heat exchanger is considered. The Wilson plot is constructed by plotting the measured total heat transfer resistance, R_{tot}, as a function of the local resistance, R_c, as calculated by the Dittus-Boelter correlation. Lines may be fit to each data set, where the slope is the ratio, $h_0A_0/\eta hA$, and the intercept is $R_h + R_w$. A slope of 1 indicates that the experimental data agrees with the value predicted by the Dittus-Boelter correlation. A slope less than 1 indicates that the heat transfer is greater, while a slope greater than 1 indicates that the heat transfer has decreased.

A Wilson plot is displayed in Fig. 8 for results obtained at test condition I (refer to Table 3). The uncertainty in the overall thermal resistance is 5% (95% confidence interval). Error bars are shown on all data sets except for Tube Designs B and C where they are smaller than the size of the markers. Results for the conventional tube, the finless AM tube, and Tube Designs A, B, and C are shown. A linear fit to the conventional tube data with a slope near 1 (1.03) shows that the Dittus-Boelter correlation predicts the tube side heat transfer coefficient within 4% over Re_D ranging from 79 k to 246 k at test condition I. At test condition II, a similar plot (not shown here) shows that the Dittus-Boelter correlation

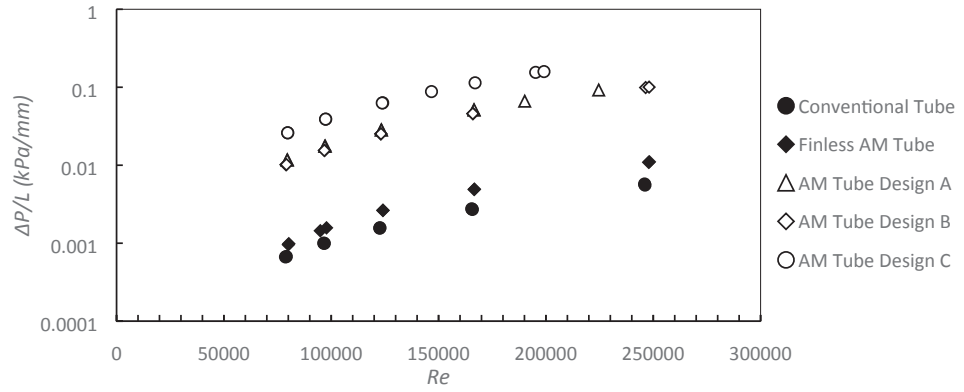

Fig. 9. Pressure drop per unit length ($\Delta P/L$) for varying $\boldsymbol{Re_D}$.

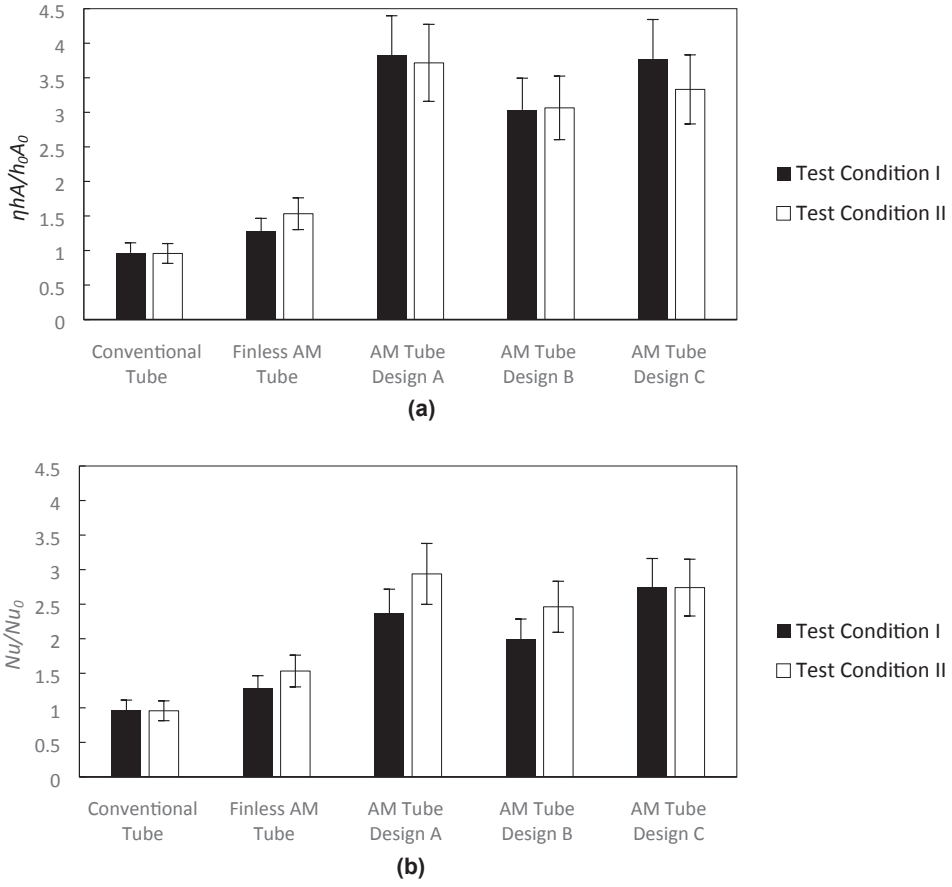

Fig. 10. (a) Heat transfer enhancement, $\eta hA/h_0A_0$, at test condition I and test condition II (b) Nu/Nu_0 ratio at the same test conditions.

predicts the tube side heat transfer coefficient within 5% over Re_D ranging from 72 k to 238 k. Both results demonstrate that the Dittus-Boelter correlation is well within the 95% confidence interval for the experimental data (±15%).

In Fig. 9, pressure drop per unit length (kPa/mm) is shown at different Re_D for each tube design considered in this study. The AM Tube Designs, A, B, and C have an order of magnitude larger pressure drop per unit length, with Tube Design C having the largest pressure drop per unit length. Tube C has the largest pressure drop because the pins are longer than the fins of Tubes A and B. Tubes A and B have similar pressure drops despite having different diameter pin fins but the same non-dimensional pitch. This is due to a higher number of pins per axial length for Tube B than Tube A. The uncertainty in the pressure drop per unit length, ±0.5% (95% confidence interval), yields error bars that are smaller than the size of the markers and thus these error bars are not shown.

3.2. Heat transfer enhancement

The heat transfer enhancement, $\eta hA/h_0A_0$, at test condition I and test condition II is plotted in Fig. 10 panel (a) for each tube design listed on the horizontal axis. $\eta hA/h_0A_0$ represents the increase in heat transfer per unit log mean temperature difference in the finned tubes relative to the heat transfer in the smooth tube, where h_0 is calculated with the Dittus-Boelter correlation. For the finned tubes, the increase is nominally threefold. At test condition I, $\eta hA/h_0A_0$ increases by 282%, 278%, and 204%, for Tube Designs A, C, and B, respectively. At test condition II, $\eta hA/h_0A_0$ increases by 271%, 233%, and 206%.

The uncertainty in the results has been reported with error bars on the $\eta hA/h_0A_0$ data. These error bars represent the 95% confidence interval for the measured results (±15%). $\eta hA/(hA)_0$ varies between test condition I and test condition II. However, this variation is on the order of the measurement uncertainty and can be neglected.

Having ruled out the variation between test condition I and test condition II, attention is now turned to variation between the AM tube designs. Tube Design B has a heat transfer enhancement that is less than Tube Design A by 15%. $\eta hA/(hA)_0$ is smaller for Tube Design B because the fin efficiency is smaller for this design. The variation in $\eta hA/h_0A_0$ between AM Tube Design A and AM Tube Design C is within the experimental uncertainty.

As a final observation, the finless AM tube has a larger heat transfer rate than the conventional tube (27% at test condition I and 56% at test condition II) but less than the finned designs. This can be attributed to the surface roughness. It must be noted that the analysis estimates the surface area of the rough AM tube to be the same as the smooth tube.

$\eta hA/h_0A_0$ may increase due to an increase in the heat transfer coefficient, the heat transfer area, or the surface efficiency. To differentiate between the increase due to the heat transfer coefficient and the increase due to the surface area and surface efficiency, $Nu/Nu_0 = h/h_0$ is plotted in Fig. 10 panel (b). The Nusselt number ratio is valuable because it represents how much advection has increased through the addition of the pin fins. It must be kept in mind that Nu/Nu_0 is equal to $\eta hA/h_0A_0$ for the conventional tube and the finless AM tube. As listed in Table 1, the area ratios for Tube Design A, B, and C are 1.8, 1.8, and 2.32 respectively. Iteratively solving for η and Nu/Nu_0 yields values for Nu/Nu_0 (panel (b)) that are less than values for $\eta hA/h_0A_0$ (panel (b)).

The uncertainty in the results has been reported with error bars on the Nu/Nu_0 data. The error bars represent the 95% confidence interval for the measured results (±15%). Nu/Nu_0 varies between test condition I and test condition II. However, this variation is on the order of the measurement uncertainty and can be neglected. Attention is now turned to the variation in Nu/Nu_0 between the tube designs. Similar to the observations made for $\eta NuA/\eta Nu_0A_0$, Tubes A and C have Nu/Nu_0

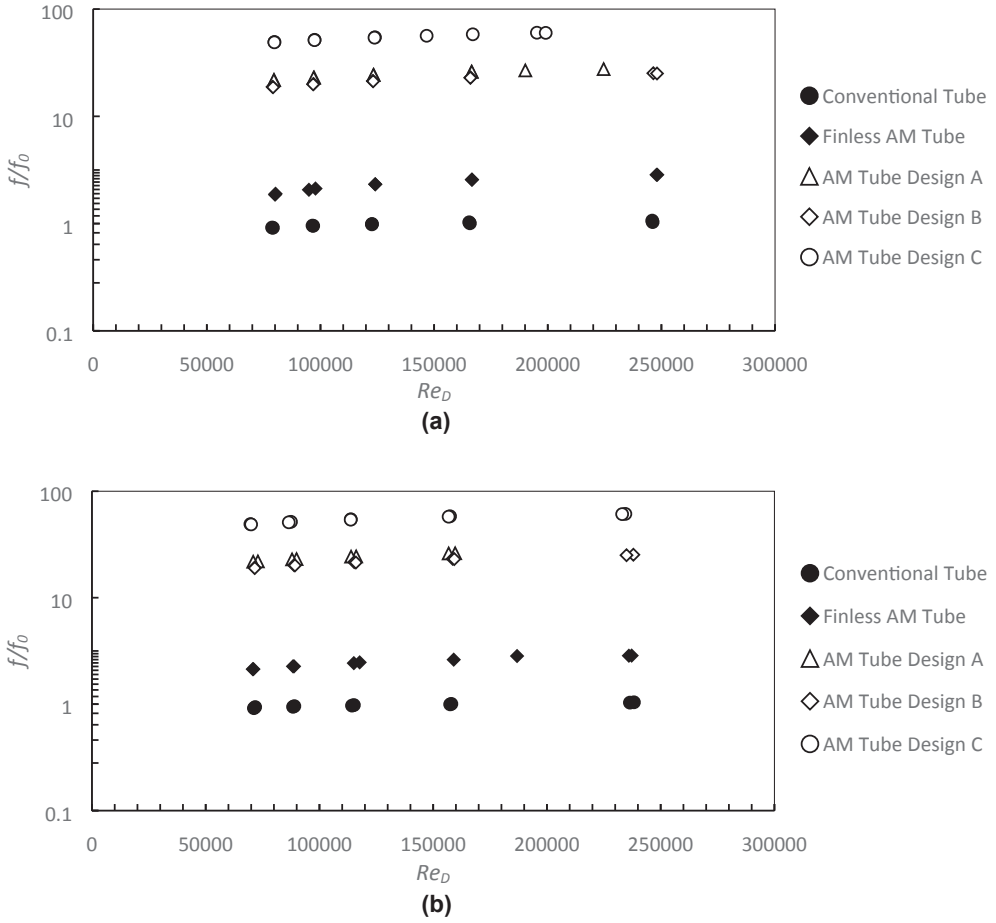

Fig. 11. (a) Friction factor ratio for varying Re_D at test condition I (b) Friction factor ratio for varying Re_D at test condition II.

values equal within experimental uncertainty and Tube B has a smaller value by 15%. The effect of area dominates the effect of surface efficiency. This is visible in the uniform decrease in value for each tube observed when comparing the plot of $\eta NuA/Nu_0A_0$ and the plot of Nu/Nu_0. The decrease would be nonuniform if surface efficiency varied significantly. Slight variation in Nu/Nu_0 between test condition I and test condition II arise as measurement uncertainty amplifies in the iterative process of calculating η and Nu.

3.3. Friction factor and thermal performance factor

While the increase in $\eta hA/h_0A_0$ and Nu/Nu_0 shown in the previous section is encouraging, this enhancement must be weighted by the increase in the friction factor when considering the thermal performance of the tube designs. Shown in Fig. 11 panels (a) and (b) are the results for f/f_0 at test conditions I and II, respectively. The uncertainty in f/f_0 is ± 5% (95% confidence interval) and is less than the size of the markers, thus error bars are not shown. The friction factors for the conventional tube agree within 3% with the McAdams correlation at test conditions I and II. The finless AM tube has friction factors 134% and 148% larger than the McAdams correlation at test conditions I and II, respectively.

A correlation is available to back out the relative roughness based on the measured friction factor and Reynolds number [18].

$$\frac{\in}{D} = 3.7\left(10^{\frac{1}{-1.8\sqrt{f}}} - \frac{6.9}{Re}\right)^{\frac{1}{1.11}} \tag{17}$$

These friction factors correspond to a relative surface roughness of 0.0046 and nominal "sand grain" roughness, $\in$, of 33 μm which is 50% larger than the R_z roughness reported by a profilometer in Section 2.3. The sand grain roughness can deviate from the measured roughness as the sand grain roughness was determined for surfaces artificially roughened with glued sand grains, while the profilometer results measure the roughness of the actual surfaces utilized in these studies. A correlation is required to relate the "sand grain roughness" to measured surface roughness but the roughness considered here is lower than the range of available correlations [14].

The finned tube designs have friction factors an order of magnitude larger than the smooth tube correlation (nominally 2300%). Further, Tube Design C has a friction factor twice as large as Tube Designs A and B. While several parameters change between Tube Design C and Tube Design A, the cause for the increase in the friction factor is the increase in the length of the pin fins, since the longer pin fins dramatically decrease the flow area. The performance of Tube Design C may be improved by decreasing the length of the fins.

Tube Design A has an f/f_0 that is slightly larger than Tube Design B. This corresponds to the larger Nusselt number for Tube Design A than Tube Design B, where the increase is expected from the Reynolds analogy.

The Nusselt number and friction factor ratios are used to determine how much material could be reduced by replacing the smooth tubes with finned tubes. This is done under the constraint of equal heat duty and pumping power. The performance factor to minimize material volume, V/V_0, was given in Eq. (11) [20]. If $V/V_0 < 1$, a heat exchanger constructed with the finned tube design will require less material than a heat exchanger constructed with finless tube under the same constraints. V/V_0 is plotted as a function of Reynolds number in Fig. 12 at test conditions I and II, panels (a) and (b), respectively. Results are shown for the tubes listed in the figure legends. At both test conditions, the results for the conventional tube deviate by no more than ± 10% from V/V_0 =

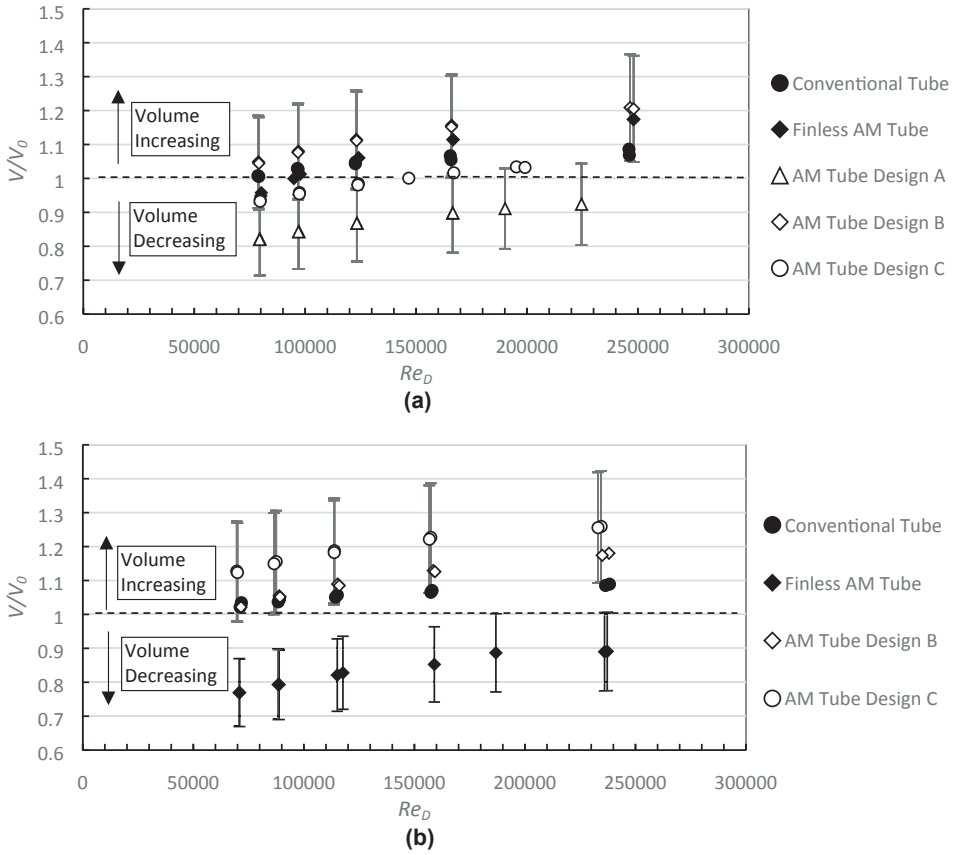

Fig. 12. (a) The thermal performance factor (V/V_0) for varying Re_D at test condition I (b) V/V_0 for varying Re_D at test condition II.

1. This is within the 95% confidence interval for the experimental data (±13%).

The best performing design is Tube Design A which yields an average V/V_0 of 0.87 at test condition I. This indicates that a heat exchanger composed of Tube Design A would require 13% less material, than a heat exchanger manufactured with smooth tubes. The reduction in tube

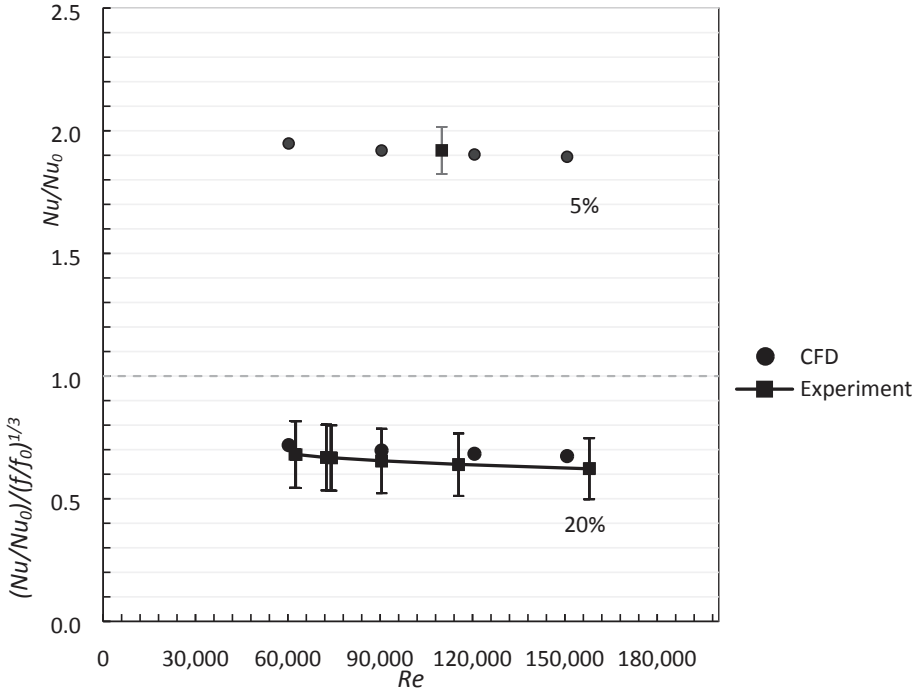

Fig. 13. The Nusselt number enhancement, Nu/Nu_0, and the classical thermal performance factor, $(Nu/Nu_0)/(f/f_0)^{1/3}$, as a function of the Reynolds number, Re, for CFD and experimental results for Tube B.

material is due to the pin fins causing a sufficiently large increase in Nu/Nu_0, relative to the increase in f/f_0, to yield a decrease in V/V_0. Test condition II for Tube Design A is not displayed since it is an outlier, resulting from measurement uncertainties amplified by the iterative process of calculating the Nusselt number and surface efficiency.

Tube Designs B and C perform poorly at both test conditions requiring 10%-20% more material on average. Tube Design B requires more heat exchanger material because Nu/Nu_0 is less than Tube Design A (f/f_0 is nearly equal). The lower Nu/Nu_0 results from the greater number of smaller pin fins. Tube Design C requires more heat exchanger material because f/f_0 is much greater than f/f_0 for Tube Design A (Nu/Nu_0 is equal within uncertainty) and the larger f/f_0 results from the increased blockage due to the longer pin fins.

A heat exchanger constructed with the finless AM tube requires more material than the conventional tube at test condition I ($V/V_0 = 1$) but requires 17% less material than Tube Design A at test condition II. The reason for this variation is due to the closer proximity of test condition I to the critical point where greater variation of properties with pressure and temperature are observed. The decrease in required material at test condition I is attributed to the introduction of surface roughness. The surface roughness causes a sufficiently large increase in Nu/Nu_0, relative to the increase in f/f_0, to yield a decrease in V/V_0.

3.4. Companion study and future work

A companion study at NETL is seeking to reduce the material volume of pin fin designs by utilizing computational fluid dynamics (CFD) to determine Nu/Nu_0 and f/f_0 of candidate pin fin tubes. We present here a benchmark of the CFD analysis with the present experimental results.

Results obtained with CFD and experiments for helical pin fin design B are shown in Fig. 13. Here, Nu/Nu_0 and $(Nu/Nu_0)/(f/f_0)^{1/3}$ are plotted as a function of *Re*. It is important to note that the Wilson plot technique cannot measure Nu/Nu_0 at a single Reynolds number but rather measures this ratio across a range of Reynolds numbers. Thus, a single Nusselt number ratio is reported in Fig. 13 at the center of the range of Reynolds numbers (60 k to 160 k). The CFD and experimental results for Nu/Nu_0 agree within 2.5% and, thus, the CFD results lie within the 95% confidence interval for the experimental results (±5%).

However, f/f_0 may be measured at each *Re* and thus experimental results are reported for $(Nu/Nu_0)/(f/f_0)^{1/3}$at varying *Re* and use Nu/Nu_0 for the entire range at each point. The CFD and experimental results for $(Nu/Nu_0)/(f/f_0)^{1/3}$ agree within 10% and, thus, the CFD results lie within the 95% confidence interval for the experimental results (±20%).

The present experiments have provided a benchmark for the CFD studies. This benchmark increases the confidence in the CFD and the results of the optimization. When the CFD optimization concludes, the optimal candidate(s) will be printed and tested at NETL as a validation.

4. Conclusions

This work reports experiments performed in the HEET rig at the U.S. DOE's National Energy Technology Laboratory. The Wilson plot technique was utilized to measure the heat transfer coefficients in supercritical carbon dioxide flowing through additively manufactured tubing with novel helical pin fins. The following conclusions were made:

- The results for a smooth, conventional tube agreed within 5% of the Dittus-Boelter correlation and within 5% of the McAdams correlation.
- For the best performing helical pin fin design, the tube side conductance increased by 277% and the heat transfer coefficient increased by 132% relative to the Dittus-Boelter correlation.
- Across the range of Re_D considered (7×10^4 to 2.5×10^5), the average friction factor increased by 2300% relative to the McAdams correlation.
- Using conventional heat exchanger scaling relations for constant heat duty and pumping power, the heat exchanger fabricated with the pin fin design (Design A) will require 10% less material than the heat exchanger fabricated with the smooth tubes.
- The Nusselt number measured in the present study agreed within 2.5% of the Nusselt number calculated in a companion CFD study.

Declaration of Competing Interest

None.

Acknowledgements

The authors wish to acknowledge the contributions of Mike Ciocco, Dennis Lynch, Curtis Batton, Mark Tucker, Jeff Riley, and Rich Eddy for their meticulous efforts in reviewing and modifying the design, constructing the test rig, designing the instrumentation and control system, developing the test procedure, and collecting experimental data. The authors would also like to thank Keith Carver and Fred List III of ORNL for providing AM design support and printing the test articles. The authors would like to thank Tim Ford for the photo of the test articles.

This research was supported by the Turbines Program of the National Energy Technology Laboratory (NETL) of the U.S. Department of Energy. This effort was also sponsored, in part, by an appointment to the U. S. Department of Energy Postgraduate Research Program at the NETL and administered by the Oak Ridge Institute for Science and Education (ORISE).

Appendix A:. Surface roughness parameters

Surface roughness characterization of AM surfaces was well-defined in a paper by Stimpson et al. [14]. Five roughness parameters were defined: arithmetic mean roughness, R_a, root-mean-square roughness, R_q, mean roughness depth, R_z, skewness, R_{sk}, and kurtosis, R_{ku}. The expressions for these

roughness parameters are repeated here and their significance explained.

$$R_a = \frac{1}{n}\sum_{i=1}^{n}|z_i - \mu| \tag{A.1}$$

$$R_q = \sqrt{\frac{1}{n}\sum_{i=1}^{n}(z_i - \mu)^2} \tag{A.2}$$

$$R_z = \frac{1}{n}\sum_{i=1}^{n}(z_{max} - z_{min})_i \tag{A.3}$$

$$R_{sk} = \frac{1}{nR_q^3}\sum_{i=1}^{n}(z_i - \mu)^3 \tag{A.4}$$

$$R_{ku} = \frac{1}{nR_q^4}\sum_{i=1}^{n}(z_i - \mu)^4 \tag{A.5}$$

where z_i are profile heights along a surface roughness profile, μ is the mean height, z_{min} is the minimum height, z_{max} is the maximum height, and n is the number of points along the profile.

R_a is the arithmetic average roughness and is a measure of the average variation of the roughness profile about the mean. R_q is the root-mean-square roughness and is a measure of the variation of the roughness profile about the mean, but unlike the arithmetic roughness weights larger variations more than smaller variations. R_z is the mean roughness depth and can be defined in different ways. Here it is defined as the average of the maximum minus the minimum height for five different regions along the profile. R_{sk} is the skewness and is a measure of how the data are distributed about the mean. A positive skewness means there are more peak-like features while a negative skewness means that there are more valley-like features. R_{ku} is the kurtosis and is a measure of the width of the roughness distribution relative to a Gaussian distribution. A large kurtosis implies that the height changes rapidly and has sharp features while a small kurtosis implies that the height changes slowly and has smooth features.

Appendix B:. Thermal performance factor derivation

Webb and Scott previously derived a thermal performance factor to minimize heat exchanger tube material volume, V, under the constraint of equal heat duty per unit log mean temperature difference, UA, and equal pumping power, P [19–20]. Their solution is reproduced here with minor modifications.

In many heat exchangers, it is reasonable to assume negligible wall resistance. The overall thermal resistance in a heat exchanger composed of smooth tubes and having negligible wall resistance may be expressed, as:

$$\frac{1}{U_s A_s} = \frac{1}{h_s A_s} + \frac{1}{h_{0s} A_{0s}} \tag{B.1}$$

where U is the overall heat transfer conductance, A is the heat transfer area, and h is the heat transfer coefficient. The subscript "s" indicates a smooth, finless tube and the subscript "0" indicates the outer surface. Equation (B.1) can be written

$$\frac{1}{U_s A_s} = \frac{1}{h_s A_s}(1 + r) \tag{B.2}$$

where $r = h_s A_s/(h_{0s} A_{0s})$. For a heat exchanger composed of internally finned tubes

$$\frac{1}{UA} = \frac{1}{\eta h A} + \frac{1}{h_0 A_0} \tag{B.3}$$

where the lack of a subscript, "s", indicates a finned tube and η is the overall surface efficiency. The surface area ratio A/A_s is defined by

$$\frac{A}{A_s} = \frac{NL}{(N_s L_s)}(A_a/A_n) \tag{B.4}$$

where N is the number of flow circuits in parallel, L is the length of each flow circuit, A_a is the finned tube internal surface area per unit length, and A_n is the smooth tube surface area per unit length. Since A/A_s equals A_a/A_n, when $NL = N_s L_s$, $A_s A_a/(AA_n) = 1$, multiplying Eq. (B.3) by $A_s A_a/(AA_n)$ yields

$$\frac{A_s A_a}{AA_n}\frac{1}{UA} = \frac{A_s A_a}{AA_n}\frac{1}{hA} + \frac{A_s A_a}{AA_n}\frac{1}{h_0 A_0} \tag{B.5}$$

Which may be simplified to

$$\frac{1}{UA} = \frac{1}{\eta h A} + \frac{A_s A_a}{h_0 A_0 A A_n} \tag{B.6}$$

There is no added surface at the tube outer wall, thus $h_0 = h_{0s}$ and $A_0 = A_{0s}$. Making this substitution yields

$$\frac{1}{UA} = \frac{1}{\eta h A} + \frac{A_s A_a}{h_{0s} A_{0s} A A_n} \tag{B.7}$$

Factoring out $1/hA$ yields

$$\frac{1}{UA} = \frac{1}{hA}\left(\frac{1}{\eta} + \frac{A_s A_a hA}{h_{0s} A_{0s} A A_n}\right) \tag{B.8}$$

Rearranging yields

$$\frac{1}{UA} = \frac{1}{hA}\left(\frac{1}{\eta} + \frac{h_s A_s}{h_{0s} A_{0s}} \frac{hA_a}{h_{sA_n}}\right) \tag{B.9}$$

r may be substituted for $h_s A_s/(h_{0s} A_{0s})$ yielding

$$\frac{1}{UA} = \frac{1}{hA}\left(\frac{1}{\eta} + r\frac{hA_a}{h_s A_n}\right) \tag{B.10}$$

Combining Eqs. (B.2) and (B.10) yields

$$\frac{UA}{U_s A_s} = \frac{\left(\frac{A}{A_s}\right)(1+r)}{\left(\frac{h_s}{\eta h} + \frac{rA_a}{A_n}\right)} \tag{B.11}$$

The heat transfer coefficient can be written in terms of the Stanton number

$$\frac{h}{h_s} = \frac{St}{St_s}\left(\frac{G}{G_s}\right) \tag{B.12}$$

where $St = h/Gc_p$, G is the tube mass flux, and c_p is the tube specific heat at constant pressure.
Substituting Eq. (B.12) into Eq. (B.11) yields

$$\frac{UA}{U_s A_s} = \frac{\left(\frac{A}{A_s}\right)(1+r)}{\left(\frac{St_s G_s}{\eta St G} + \frac{rA_a}{A_n}\right)} \tag{B.13}$$

The friction power ratio of the internally finned and smooth tube heat exchangers is

$$\frac{P}{P_s} = \frac{f}{f_s}\frac{A}{A_s}\left(\frac{G}{G_s}\right)^3 \tag{B.14}$$

where f is the Fanning friction factor. Eliminating G/G_s by combining Eqs. (B.13) and (B.14) yields

$$\frac{UA}{U_s A_s} = \frac{1+r}{\frac{1}{\eta}\left[\frac{\frac{f}{f_s}}{\left(\frac{P}{P_s}\right)\left(\frac{A}{A_s}\right)^2}\right]^{\frac{1}{3}}\left(\frac{St_s}{St}\right) + \frac{r\left(\frac{A_a}{A_n}\right)}{\frac{A}{A_s}}} \tag{B.15}$$

The surface area ratio A/A_s is defined by

$$\frac{A}{A_s} = \frac{NL}{(N_s L_s)}(A_a/A_n) \tag{B.16}$$

where N is the number of flow circuits in parallel and L is the length of each flow circuit.
Defining M as the tube material volume per unit length,

$$\frac{V}{V_s} = \frac{NL}{N_s L_s}\frac{M}{M_s} \tag{B.17}$$

Combining Eqs. (B.16) and (B.17) yields,

$$\frac{V}{V_s} = \frac{M}{M_s}\frac{A}{A_s}\frac{A_n}{A_a} \tag{B.18}$$

Simplifying assumptions and constraints are now applied to Eq. (B.15). First, enhancing a heat transfer surface with fins is most beneficial when the thermal resistance on that side of the heat exchanger is large. Thus, we assume that the thermal resistance of the outer heat exchanger surface is small. This requires that $r = h_s A_s/(h_{0s} A_{0s})$approach zero. Next, we constrain the smooth tube and finned tube heat exchangers so that they have equal heat duty and receive equal pumping power. Making these substitutions yields

$$1 = \frac{1}{\frac{1}{\eta}\left[\frac{\frac{f}{f_s}}{\left(\frac{A}{A_s}\right)^2}\right]^{\frac{1}{3}}\left(\frac{St_s}{St}\right)} \tag{B.19}$$

Solving for A/A_s yields

$$\frac{A}{A_s} = \frac{\left(\frac{f}{f_s}\right)^{\frac{1}{2}}}{\left(\eta\frac{St}{St_s}\right)^{\frac{3}{2}}} \tag{B.20}$$

We substitute this result into Eq. (B.18) yielding

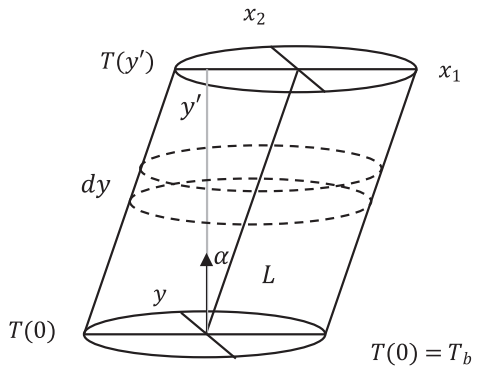

Fig. C1. An elliptical pin fin is shown with dimensions.

$$\frac{V}{V_s} = \frac{M}{M_s}\frac{A_n}{A_a}\frac{\left(\frac{f}{f_s}\right)^{\frac{1}{2}}}{\left(\eta\frac{St}{St_s}\right)^{\frac{3}{2}}} \tag{B.15}$$

$V/V_s < 1$indicates that a heat exchanger fabricated with finned tubes will require less material than a heat exchanger fabricated with smooth tubes when the heat exchangers are constrained to have the same heat duty and pumping power.

Appendix C:. Angled pin fin efficiency

The efficiency of an angled elliptical pin fin, η_f, was derived by a co-author (Ed Robey). In Fig. C1, a single pin fin is displayed. The pin length is L and the angle from the vertical is α. The pin vertical height is y' and x_1 and x_2 are the semimajor and semiminor radii, respectively.

A control volume is obtained which is differential in the y-axis and a heat conduction balance is performed

$$\dot{Q}(y+dy) = \dot{Q}(y) + d\dot{Q}_{conv} \tag{C1}$$

By Newton's law of cooling

$$d\dot{Q}_{conv} = hdA_s(T - T_\infty) \tag{C2}$$

where h is the heat transfer coefficient and dA_s is the differential surface area.

The perimeter, P, and surface area, A_s, are

$$A_s = \frac{\sqrt{2}\pi y' x_1\sqrt{\cos^2(\alpha) + (x_2/x_1)^2}}{\cos(\alpha)} \tag{C3}$$

and

$$P = \sqrt{2}\pi x_1\sqrt{1 + \left(\frac{x_2}{x_1}\right)^2} \tag{C.4}$$

Dividing Eq C.4 by Eq. C.3 and taking the differential yields

$$dA_s = dyP\sqrt{\frac{1 + (x_2/x_1)^2/\cos^2(\alpha)}{1 + (x_2/x_1)^2}}$$

Substituting this result into equation C.2 yields

$$\dot{Q}(y+dy) = \dot{Q}(y) + hdyP\sqrt{\frac{1 + (x_2/x_1)^2/\cos^2(\alpha)}{1 + (x_2/x_1)^2}}(T - T_\infty) \tag{C.5}$$

Fourier's law yields

$$\dot{Q}(y) = -kA_c\left(\frac{dT}{dy}\right)\cos(\alpha) \tag{C.6}$$

where the $\cos(\alpha)$ results from the conduction path no longer being perpendicular to the pin axis.

Substituting from (C.6) and dividing by dy yields

$$kA_c\cos(\alpha)\frac{\left[\left(\frac{dT}{dy}\right)\Big|_{y+dy} - \left(\frac{dT}{dy}\right)\Big|_{y}\right]}{dy} = hP\sqrt{\frac{1 + (x_2/x_1)^2/\cos^2(\alpha)}{1 + (x_2/x_1)^2}}(T - T_\infty) \tag{C.7}$$

Defining $\theta(y) = T(y) - T_\infty$for $0 \le y \le y$' and

$$M^2 = \frac{Ph}{kA_c\cos(\alpha)}\sqrt{\frac{1+(x_2/x_1)^2/\cos(\alpha)^2}{1+(x_2/x_1)^2}} \tag{C.8}$$

Substituting these equations into Eq. (C.7) yields

$$\frac{d^2\theta(y)}{dy^2} - M^2\theta(y) = 0 \tag{C.9}$$

after the definition of a derivative is applied and Eq (C.8) is substituted
The boundary conditions are

$$\text{BC1}: \theta(0) = T_b - T_\infty$$

$$\text{BC2}: \dot{Q}(y') = -kcos(\alpha)A_c\left(\frac{d\theta(y)}{dy}\right)_{y=y'} = hA_c\theta(y')$$

Solving this system yields a fin efficiency of

$$\eta_f = \frac{1}{My'}\frac{\left(\sinh(My') + \frac{k\cos(\alpha)M}{h}\cosh(My')\right)}{\left(\cosh(My') + \frac{k\cos(\alpha)M}{h}\sinh(My')\right)} \tag{C.10}$$

References

[1] V. Bush, GTI STEP forward on sCO2 Power, 6th Int. sCO2 Power Cycle Symposium, Pittsburgh, PA, 2018.
[2] C.W. White, W.W. Shelton, N.T. Weiland, T.R. Shultz, sCO2 Cycle as an Efficiency Improvement Opportunity for Air-fired Coal Combustion, in: 6th Int. sCO2 Power Cycle Symposium, Pittsburgh, PA, 2018.
[3] C.W. White, N.T. Weiland, Preliminary Cost and Performance Results for a Natural Gas-fired Direct sCO2 Power Plant. 6th Int. sCO2 Power Cycle Symposium, 2018.
[4] J. Black, D. Straub, E. Robey, J. Yip, S. Ramesh, A. Roy, M. Searle, Measurement of Convective Heat Transfer Coefficients with Supercritical CO2 using the Wilson-Plot Technique, in: The 44th International Technical Conference on Clean Energy, Clearwater, Florida, USA, 2019.
[5] A.A. Gkountas, A.M. Stamatelos, A.I. Kalfas, Recuperators investigation for high temperature supercritical carbon dioxide power generation cycles, Appl. Therm. Eng. 125 (2017) 1094–1102.
[6] J. Zhou, K. Cheng, H. Zhang, B. Liu, X. Huai, J. Guo, H. Zhang, X. Cui, Test platform and experimental test on 100 kW class Printed Circuit Heat Exchanger for Supercritical CO_2 Brayton Cycle, Int. J. Heat Mass Transf. 148 (2020), 118540.
[7] L. Chai, S.A. Tassou, A review of printed circuit heat exchangers for helium and supercritical CO2 Brayton cycles, Therm. Sci. Eng. Prog. 18 (2020) 10054.
[8] Y. Jiang, E. Liese, S.E. Zitney, D. Bhattacharyya, Design and dynamic modeling of printed circuit heat exchangers for supercritical carbon dioxide Brayton power cycles, Appl. Energy 231 (2018) 1019–1032.
[9] Y. Jiang, E. Liese, S.E. Zitney, D. Bhattacharyya, Optimal design of microtube recuperators for an indirect supercritical carbon dioxide recompression closed Brayton cycle, Appl. Energy 216 (2018) 634–648.
[10] High temperature heat exchanger design and fabrication for systems with large pressure differentials. Thar Energy, LLC, Pittsburgh, PA (United States), 2017.
[11] E.E. Wilson, A basis for rational design of heat transfer apparatus, Trans. ASME 37 (1915).
[12] D.E. Briggs, E.H. Young, Modified Wilson-Plot Techniques for Obtaining Heat Transfer Correlations for Shell and Tube Heat Exchangers, Chem. Eng. Prog. Sym. Ser., 35–45, 1969.
[13] J. Fernández-Seara, F.J. Uhía, J. Sieres, A. Campo, A general review of the Wilson plot method and its modifications to determine convection coefficients in heat exchange devices, Appl. Therm. Eng. 27 (2007) 2745–2757.
[14] C.K. Stimpson, J.C. Snyder, K.A. Thole, D. Mongillo, Scaling Roughness Effects on Pressure Loss and Heat Transfer of Additively Manufactured Channels, J. Turbomach. 139 (2016), 021003.
[15] F.P. Incropera, D.P. Dewitt, T.L. Bergman, A.S. Lavine, Fundamentals of Heat and Mass Transfer, 6 ed., John Wiley & Sons, 2006.
[16] E.W. Lemmon, I.H. Bell, M.L. Huber, M.O. McLinden, NIST Standard Reference Database 23: Reference Fluid Thermodynamic and Transport Properties-REFPROP, National Institute of Standards and Technology, Gaithersburg, 2018.
[17] R. Span, W. Wagner, A New Equation of State for Carbon Dioxide Covering the Fluid Region from the Triple-Point Temperature to 1100 K at Pressures up to 800 MPa, J. Phys. Chem. Ref. Data 25 (1996) 1509–1596.
[18] B.R. Munson, D.F. Young, T.H. Okiishi, W.W. Huebsch, Fundamentals of Fluid Mechanics, 6 ed., John Wiley & Sons Inc, 2009.
[19] R.L. Webb, Performance evaluation criteria for use of enhanced heat transfer surfaces in heat exchanger design, Int. J. Heat Mass Transf. 24 (1981) 715–726.
[20] R.L. Webb, M.J. Scott, A Parametric Analysis of the Performance of Internally Finned Tubes for Heat Exchanger Application, J. Heat Transf.-Trans. ASME 102 (1980) 38–43.
[21] S. Kline, F. McClintock, Describing Uncertainties in Single-Sample Experiments, Mech. Eng. 75 (1953) 3–8.
[22] R.J. Moffat, Describing the uncertainties in experimental results, Exp. Therm Fluid Sci. 1 (1988) 3–17.